

The First Hillslope Thermokarst Inventory for the Permafrost Region of the Qilian Mountains

Xiaoqing Peng^{1,3}, Guangshang Yang¹, Oliver W. Frauenfeld², Xuanjia Li¹, Weiwei Tian¹, Guanqun Chen¹, Yuan Huang¹, Gang Wei¹, Jing Luo⁴, Cuicui Mu^{1,3}, Fujun Niu⁴

¹Key Laboratory of Western China's Environmental Systems (Ministry of Education), College of Earth and Environmental Sciences, Lanzhou University, Lanzhou, 730000, China

²Department of Geography, Texas A&M University, College Station, TX 77843-3147, USA

³Observation and Research Station on Eco-Environment of Frozen Ground in the Qilian Mountains, Lanzhou University, Lanzhou 730000, China

⁴State Key Laboratory of Frozen Soil Engineering, Northwest Institute of Eco-Environment and Resources, Chinese Academy of Sciences, Lanzhou 730000, China

* Corresponding author: Guangshang Yang (220220948511@lzu.edu.cn)

Abstract:

Climate warming and anthropogenic disturbances result in permafrost degradation in cold regions, including in the Qilian Mountains. These changes lead to extensive hillslope thermokarst (HT) formation, such as retrogressive thaw slumps, active-layer detachment slides, and thermal erosion gullies. These in turn cause, e.g., degradation of local vegetation, economic losses, infrastructure damages, and threats to human safety. However, despite its importance, there is currently no thermokarst inventory for the Qilian Mountains. Through manual visual interpretation and field validation, we therefore produce the first quantification of HT features. We count a total of 1064 HT features, with 67% located in the upper reaches of the Heihe River Basin, which encompasses ~13% of the Qilian Mountains region. We furthermore document that 82% of the HT was initiated in the last 10 years. The thermokarst terrain is observed primarily in areas with shallow active layer depth (average thickness: 2.98 m), on northern shaded slopes of 3–25°, with low solar radiation and moderate elevations ranging from 3200 to 4000 m. This first inventory of HT features is an important and missing piece in documenting changes on the Qinghai-Tibetan Plateau, and this new dataset also provides an important basis for further studies on, e.g., quantitative assessment losses caused by HT. The datasets are available from the National Tibetan Plateau/Third Pole Environment Data Center and can be downloaded from <https://doi.org/10.11888/Cryos.tpdc.300805> (Peng and Yang, 2023).

40 **1 Introduction**

41 The Qilian Mountains are located in the northeastern part of the Qinghai-Tibetan
42 Plateau, at the confluence of three major geographical regions that include the eastern
43 monsoon zone, the northwestern arid zone, and the alpine zone of the Qinghai-Tibetan
44 Plateau. The Qilian Mountains play an important role in maintaining the ecological
45 balance of the Tibetan Plateau, stopping the southward progression of deserts, and
46 maintaining the stability of the oases in the Hexi Corridor. Due to its unique
47 geographical and environmental characteristics, permafrost is widespread and
48 underlies about 50% of the area (Ran et al., 2021). Permafrost has an important role in
49 storing frozen water, thereby contributing to water conservation (Wang et al., 2022).
50 These roles can aid in inland river runoff recharge, which is crucial to regional
51 ecology, production, and life. Due to climate warming and human activities,
52 significant permafrost degradation results in the frequent occurrence of thermokarst,
53 representing a serious threat to ecological security and adversely impacts the
54 environment and human beings (Li et al., 2022a).

55 Despite the importance of thermokarst processes and their potential geohazards, the
56 distribution of thermokarst landscapes is currently mostly undocumented. The
57 available distribution of thermokarst in the Northern Hemisphere, including
58 retrogressive thaw slumps (RTSs), thermokarst lakes, and other terrain features,
59 represents mainly probabilistic estimates (Olefeldt et al., 2016; Yin et al., 2021;
60 Huang et al., 2023; Yang et al., 2023). Muster et al. (2017) determined the distribution
61 of circumpolar Arctic permafrost lakes and ponds from 2002–2013 at a resolution of 5
62 m using optical remote sensing, satellite (Geo-Eye, QuickBird, WorldView-1 and -2,
63 KOMPSAT-2), and radar imagery (TerraSAR-X), but temporal inconsistencies make
64 comparisons in time and space difficult. At the regional scale, the techniques and
65 spatial resolution of remote sensing imagery currently used at different study areas are
66 inconsistent, e.g., estimating the distribution and development of RTSs on Banks
67 Island, Canada, based on the interpretation of a Google Earth Engine Timelapse
68 dataset (Lewkowicz and Way, 2019). Satellite imagery at 30-m resolution from
69 Landsat has been used to analyze RTSs and thermokarst lakes in the region of Alaska
70 within the circumpolar Arctic, eastern Canada, and Siberia (Nitze et al., 2018). Nicu et
71 al. (2023) employed orthorectified imagery with a resolution of 5 meters to visually
72 interpret and identify cryospheric hazards (such as thaw slumps and thermo-erosion
73 gullies) in Nordenskiöld Land, covering an approximate area of 4000 square
74 kilometers in the Svalbard Archipelago. The permafrost zone of the Qinghai-Tibetan
75 Plateau (QTP) has been a site of thermokarst geomorphology research in recent years.
76 For example, combining field surveys and SPOT-5 satellite data for August 2010, a
77 total of 2,163 thermokarst lakes and ponds were recorded within 10 km on either side
78 of the Chumar River to Fenghuo Mountain of the Qinghai-Tibet Railway, with a total
79 surface area of $1.09 \times 10^7 \text{ m}^2$ and ranging in size from 100 m^2 to $4.49 \times 10^5 \text{ m}^2$ (Luo
80 et al., 2015; Niu et al., 2014). In the Beiluhe region of the central QTP, the number of
81 RTSs increased from 124 to 438 between 2008 and 2017, with an approximate 9-fold
82 increase in area (Huang et al., 2020; Luo et al., 2019). The latest results show that the
83 number of RTSs on the QTP is 2669, but for the Qilian Mountains in the northeastern
84 part of the region, only 6 (Luo et al., 2022) or as many as 15 are documented (Mu et
85 al., 2020). A lack of a thermokarst inventory in this region is therefore evident,
86 representing a crucial gap in the RTSs inventory on the QTP.

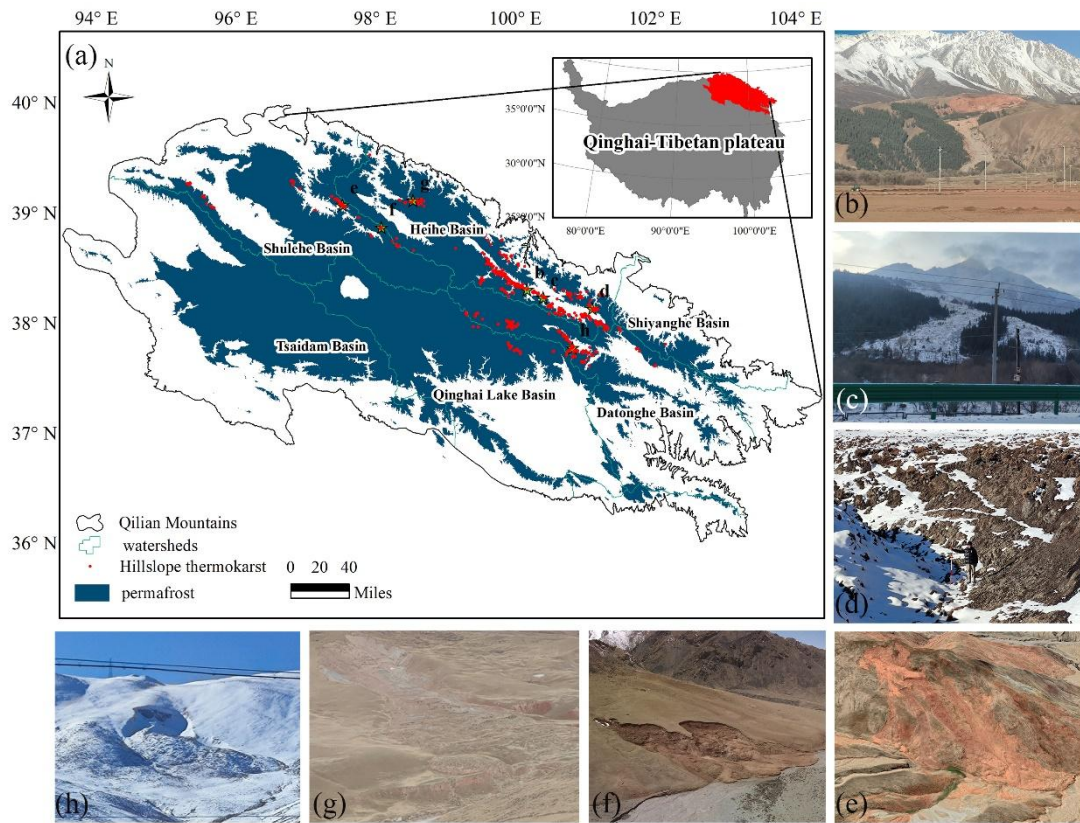
87 Frequent occurrence of hillslope thermokarst hazards due to permafrost degradation,

88 with significant ecological impacts on the Qilian Mountains. The ecological
89 environment of the permafrost areas has a significant impact, and there is a direct
90 correlation between human activities and major permafrost engineering problems,
91 including uneven subsidence of infrastructure, slumps, and cracks. Meanwhile, there
92 is little to no information regarding hillslope thermokarst (HT) features such as RTSs,
93 active-layer detachment slides, and thermo-erosion gullies (Gooseff et al., 2009) in
94 the Qilian Mountains. HT refers to a specific type of thermokarst formation that
95 occurs in permafrost regions. While it is similar to regular thermokarst features, what
96 distinguishes hillslope thermokarst is its occurrence on sloped terrain or hillsides,
97 where permafrost thaw leads to slope instability. This can result in various landforms
98 like retrogressive thaw sumps, thermo-erosion gullies, or active layer detachments,
99 affecting the stability and shape of hillslopes in permafrost regions. These features can
100 significantly impact the landscape and have implications for infrastructure,
101 ecosystems, and land use in areas affected by hillslope thermokarst processes (Kokelj
102 and Jorgenson, 2013; Olefeldt et al., 2016; Gooseff et al., 2009). Thus, the urgent need
103 to survey and quantify these undocumented HTs in the Qilian Mountains motivates
104 and represents the goal of this study.

105

106 **2 Study Area**

107 The Qilian Mountains are located at the northern edge of the QTP, with an average
108 elevation of 3855 m. The region is underlain by permafrost and seasonally frozen
109 ground (36–40°N and 94–104°E, Figure 1a), with a permafrost area of 94,235 km²
110 that accounts for 49% of the study domain. Characterized by both an alpine mountain
111 climate and a temperate continental monsoon climate, the mean annual air
112 temperature is 0.30°C (Jin et al., 2022) with high precipitation variability and higher
113 amounts in the southeast during the thawing season of June to September (Chen et al.,
114 2013; Li et al., 2022b). Due to human activities, climate change, and earthquakes,
115 permafrost instability in Qilian Mountains has gradually increased, resulting in HT
116 formation including RTSs, active-layer detachment slides, and thermal erosion gullies,
117 which pose a direct threat to the local economy, ecology, and safety.



118

119 **Figure 1** The location of the study area and a) its HT distribution (Qilian Mountains
 120 permafrost extent data is from Sheng et al., 2020), and b)–h) HT features obtained
 121 from different watersheds during our field surveys with the exception of e) a Google
 122 Earth image, as this site is too difficult to access, the positions corresponding to b)–h)
 123 have been labeled in a).

124

125 3 Data Sources

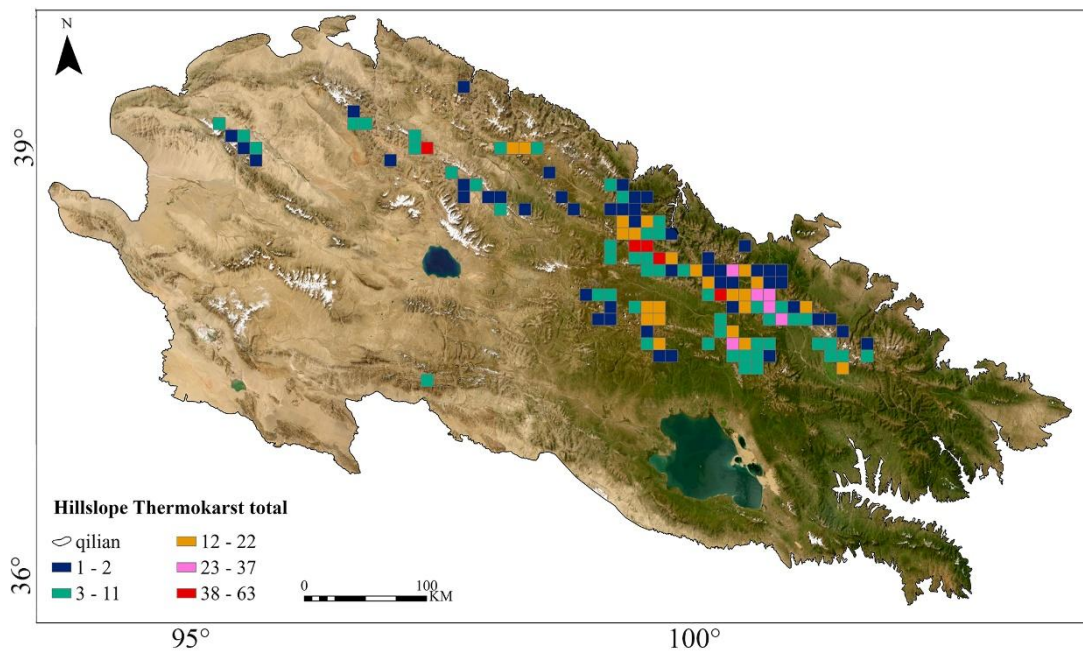
126 We collected and collated validated satellite imagery available starting in 1999 for
 127 temporal detection of the onset of the HT formation. These data include unmanned
 128 aerial vehicle imagery (e.g., Figure 1b–h) and 30 m resolution digital elevation model
 129 data from the Shuttle Radar Topography Mission (Farr et al., 2007). A combination of
 130 Omap and Google Earth software was used to detect the location of HT occurrence,
 131 and Wayback imagery provided by ESRI was used to access high-resolution (<1 m)
 132 satellite imagery and Jilin-1 satellite imagery (0.75 m) provided free of charge by
 133 China Commercial Satellite Corporation to aid in the identification (Table 1). In
 134 addition, we used digital elevation model data to calculate variables such as slope and
 135 topographic position index (TPI) of the HT. The TPI is calculated as follows (YU
 136 Hong, 2001):

$$137 \quad TPI = \log_{10} \left(\frac{E}{Mean E} + 1 \right) \times \left(\frac{S}{Mean S} + 1 \right) \quad (1)$$

138 where E is the elevation (m), S is the slope ($^{\circ}$), and $Mean$ indicates that the mean
 139 value for the entire Qilian Mountain region is used.

140 To further analyze the distribution of HT and the analogous environmental variables,
 141 We obtain seismic data from the U.S. Geological Survey
 142 (<https://earthquake.usgs.gov/earthquakes/search/>) describing earthquakes, including

143 their timing, epicenter location, and magnitude. To categorize vegetation types into
 144 deciduous-coniferous forests (DCF), undergrowth (U), alpine scrub meadow (ASM),
 145 alpine meadow (AM), alpine grassland (AG), alpine vegetation (AV), and
 146 non-vegetated area (NA), based on data from the Resource and Environment Science
 147 and Data Center (<https://www.resdc.cn/data.aspx?DATAID=122>). To assess the
 148 relationship of air temperature and precipitation with HT, we download monthly mean
 149 air temperature and precipitation at 2 m above ground level from the fifth generation
 150 of the European Centre for Medium-Range Weather Forecasts (ECMWF) reanalysis
 151 (ERA5;
 152 <https://cds.climate.copernicus.eu/cdsapp#!/dataset/reanalysis-era5-land-monthly-means?tab=overview>).
 153
 154



155
 156
 157 **Figure 2** Frequency distribution of HT on the Qilian Mountains. The concentration of
 158 HTs is shown per 100 km² grid cell.
 159

160 4 Methods

161 4.1 Manual Mapping

162 We first quantified and mapped HT via remote sensing observations. Most
 163 occurrences of HT in the permafrost region of the Qilian Mountains since 2000 were
 164 compiled by visual interpretation in Google Earth Pro and Omap. They were also
 165 aided by high resolution (<1 m) observations from Esri Wayback Imagery, which
 166 archives all published versions of world imagery (Table 1). We used a fishnet with a
 167 mesh size of 1×1 km to segment the latest satellite imagery for the entire Qilian
 168 Mountains to quantify HT mesh by mesh. RTSs are often horseshoe shaped, tongue
 169 shaped, elongated, branched, and circle chair-shaped (Lantuit and Pollard, 2008; Yin
 170 et al., 2021), characterized by a steep backwall, low-angle bottom, and a tongue of
 171 displaced saturated soil (Lantz and Kokelj, 2008; Nicu et al., 2021). These features are
 172 tonally and morphologically different from their surroundings in color satellite images
 173 during the thawing season. RTSs also produce folded textures due to soil

174 accumulation, which appear as laterally folded stripes on imagery. Active-layer
 175 detachment slides are a common shallow landslide in permafrost areas. Their
 176 morphological characteristics vary based on vegetation cover, slope, and permafrost
 177 conditions, but common features include highly disturbed slopes, lateral shear zones,
 178 and fracture zones formed after the sliding of the active layer. (Lewkowicz, 2007). We
 179 detected and sketched these features based on morphological, tonal, textural, shading,
 180 and other characteristics on remote sensing images, and then digitized their
 181 morphological features into polygonal data. Although the accuracy of this type of
 182 visual interpretation is relatively high, some HT features can be missed via this
 183 manual interpretation. To reduce such errors, satellite images of the similar period
 184 from different sources were evaluated four times using the same methods to ensure
 185 accurate results. The date of the satellite image when perturbations caused by HT can
 186 be first observed was defined as the initiation year of a particular HT feature.
 187 Depending on the initiation year, HT is categorized as occurring before 2010,
 188 2010–2015, or after 2015. To observe the temporal evolution of HT features, we used
 189 the initiation year and retraced historical images covering the Qilian Mountains, a
 190 process that also helped us distinguish between HT features and one-time transient
 191 landslides.

192
 193

4.2 Field Verification

194 Similar HT can have different morphological characteristics due to different triggers.
 195 It is thus difficult to identify the type of HT simply through imagery. In addition, after
 196 an initial trigger and HT formation, thermokarst can evolve into different types. For
 197 example, active layer detachment slides may transition into RTS due to the exposure
 198 of subsurface ice at the trailing edge and water erosion due to thawing, which can
 199 cause the RTS to further progress into mudflows. Therefore, with visual interpretation
 200 based on imagery only providing individual snapshots, it is essential to also conduct
 201 field surveys as a validation exercise. We conducted a total of three field surveys in
 202 winter 2022, and spring and summer of 2023. Field work covered the Shiyanghe basin,
 203 Heihe basin, Datonghe basin, Qinghai Lake basin, and Shulehe basin. Due to the
 204 harsh climatic conditions and accessibility issues in the Qilian Mountains, unmanned
 205 aerial vehicles were used to survey and verify hard-to-reach areas.
 206

207 **Table 1** List of the data used for manual interpretation and mapping for HTs.

Software Platform	Time Span	Resolution	Data Sources
Google Earth pro	1999-2022	0.6-15 m	Quickbird, IKONOS, etc.
Omap	since 2021	<1 m	GF-2
ESRI World Imagery	since 2014	<1 m	WorldView-3, WorldView-4, etc.
Jilin-1 website	2022	0.75 m	Jilin-1
UAV images	Feb., Apr., May 2023	~15 cm	Field Surveys

208
 209

4.3 Morphological and Spatial Statistical Analysis

210 A landscape shape index (LSI) can be quantified to characterize shape complexity by
 211 calculating the degree of deviation of a given patch from a circle or square of the

212 same area. To quantify the shape characteristics of HT features, two LSIs are
213 calculated as follows:

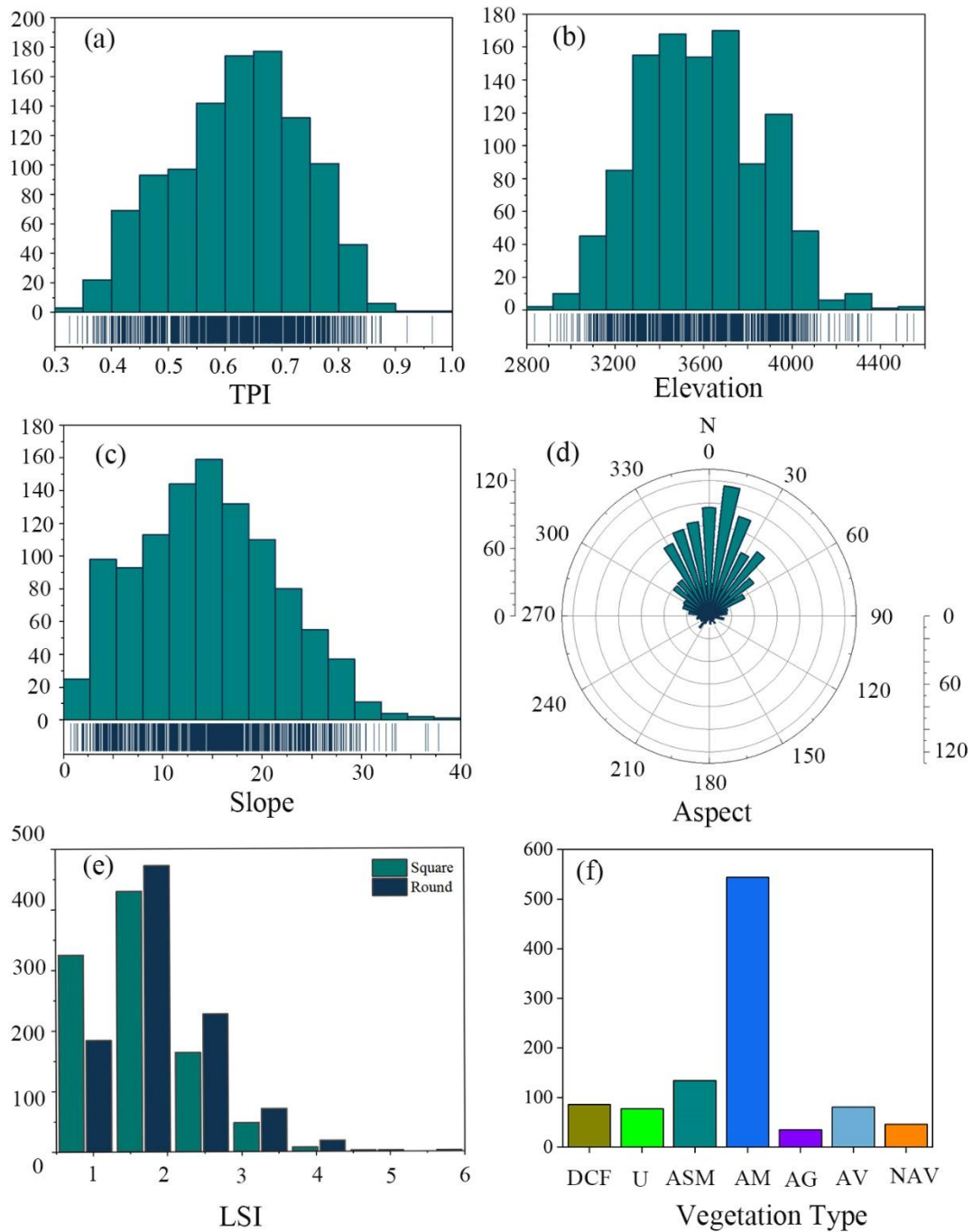
$$214 \quad LSI_{square} = \frac{0.25P}{\sqrt{A}} \quad (2)$$

$$215 \quad LSI_{round} = \frac{P}{2\sqrt{\pi A}} \quad (3)$$

216 where P is the perimeter (m) and A is the area (m²). The closer the values of LSI_{square}
217 or LSI_{round} are to 1, the more square or round the shape of the HT feature is,
218 respectively.

219 To further investigate the spatial distribution of HT, we computed a global Moran's
220 index, z-score and p-value to determine whether there is autocorrelation in the spatial
221 distribution of HT. Where p-value and z-score are used to measure statistical
222 significance, when p-value < 0.01 and z-score > 2.58, it means that there is a 99%
223 probability that HTs are clustered within the study area, and the smaller the p-value
224 and the larger the z-score, the greater the probability that such spatial patterns are
225 clustered. Moran's index ranges from -1 to 1, with negative values meaning negative
226 correlation, positive values meaning positive correlation, and 0 denotes that the spatial
227 objects in the study area are independent of each other. Additionally, the closer the
228 index is to 1, the more clustered the HT features are, and the closer of the index is to
229 -1, the more dispersed the HT features are. To delineate the regions that may have
230 spatial autocorrelation (Bivand and Wong, 2018), we further process local
231 autocorrelation on this basis. The local autocorrelation regions are divided into four
232 types: The local autocorrelation analysis categorizes regions into four types based on
233 the local Moran's index: High-High (HH) clustering, High-Low (HL) clustering,
234 Low-High (LH) clustering, and Low-Low (LL) clustering. HH signifies a region with
235 both a higher amount of HT and neighboring regions also having a higher amount of
236 HT; HL indicates a region with a higher amount of HT surrounded by neighboring
237 regions with a lower amount of HT; LH indicates a region with a lower amount of HT
238 neighboring areas with a higher amount of HT; and LL represents a region with both a
239 lower amount of HT and neighboring regions with a lower amount of HT. Although
240 the methods described above can identify global and local spatial autocorrelation,
241 respectively, they are unable to identify clusters of concentrated HT features. We
242 therefore also apply hot spot analysis, which is another effective way of exploring the
243 characteristics of local spatial distributions. All the above techniques are based on
244 spatial statistical analysis functions of ArcGIS.

245 To explore the effects of climate on HT, we obtained the monthly mean air
246 temperature and precipitation at 2 meters above ground level from ERA5 over the
247 period 2000–2020 and calculate their annual spatial means and standard deviations
248 (Figure 6).



249
 250 **Figure 3** The number of HT terrain features (y-axes) of HT as categorized by (a)
 251 topographic position index (TPI), (b) elevation, (c) slope, (d) aspect, (e) landscape
 252 shape index (LSI), and (f) vegetation type including deciduous coniferous forests
 253 (DCF), undergrowth (U), alpine scrub meadow (ASM), alpine meadow (AM), alpine
 254 grassland (AG), alpine vegetation (AV), and non-vegetated area (NA); the blue
 255 vertical lines at the bottom of panels a–c represent the number of HT features in each
 256 x-axis bin.

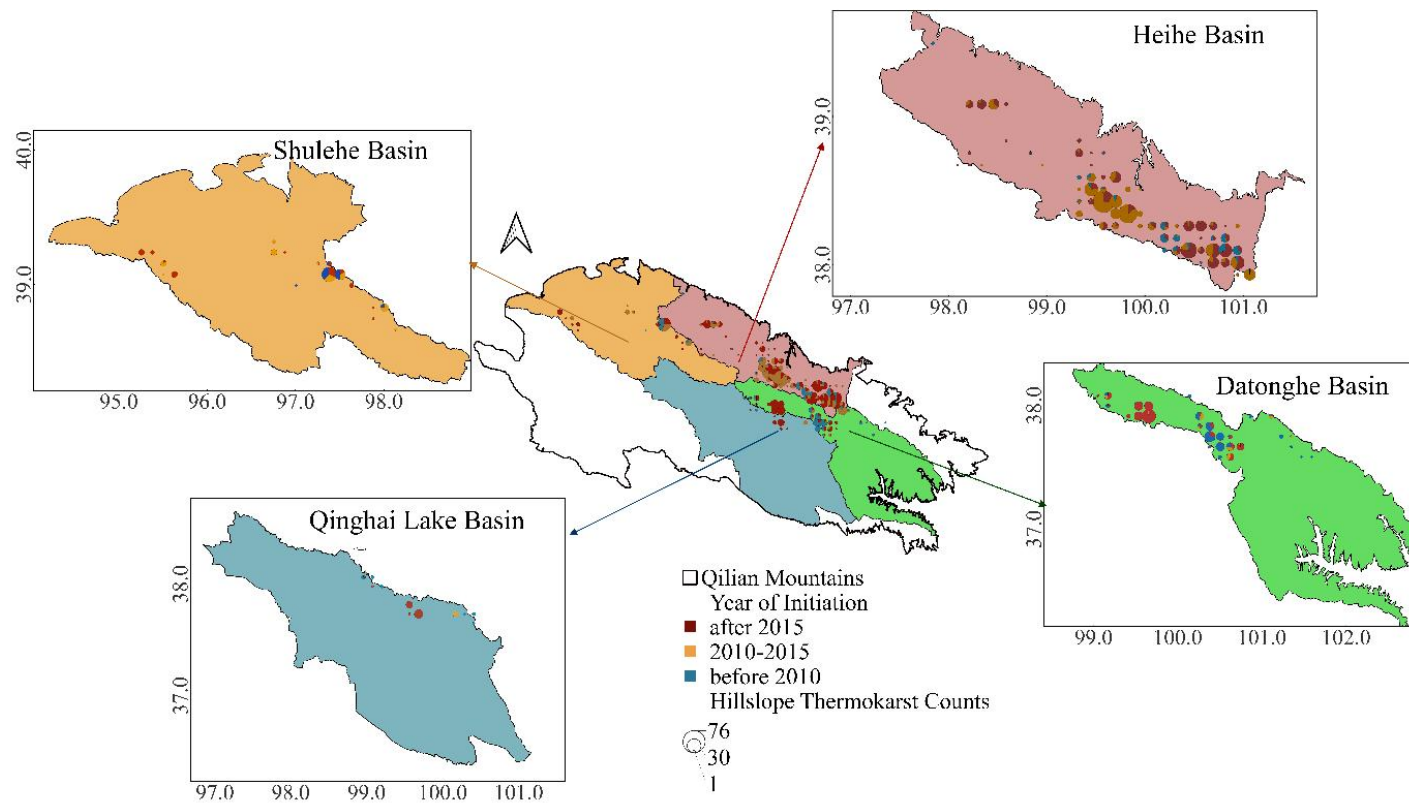
257

258 **5 Results**

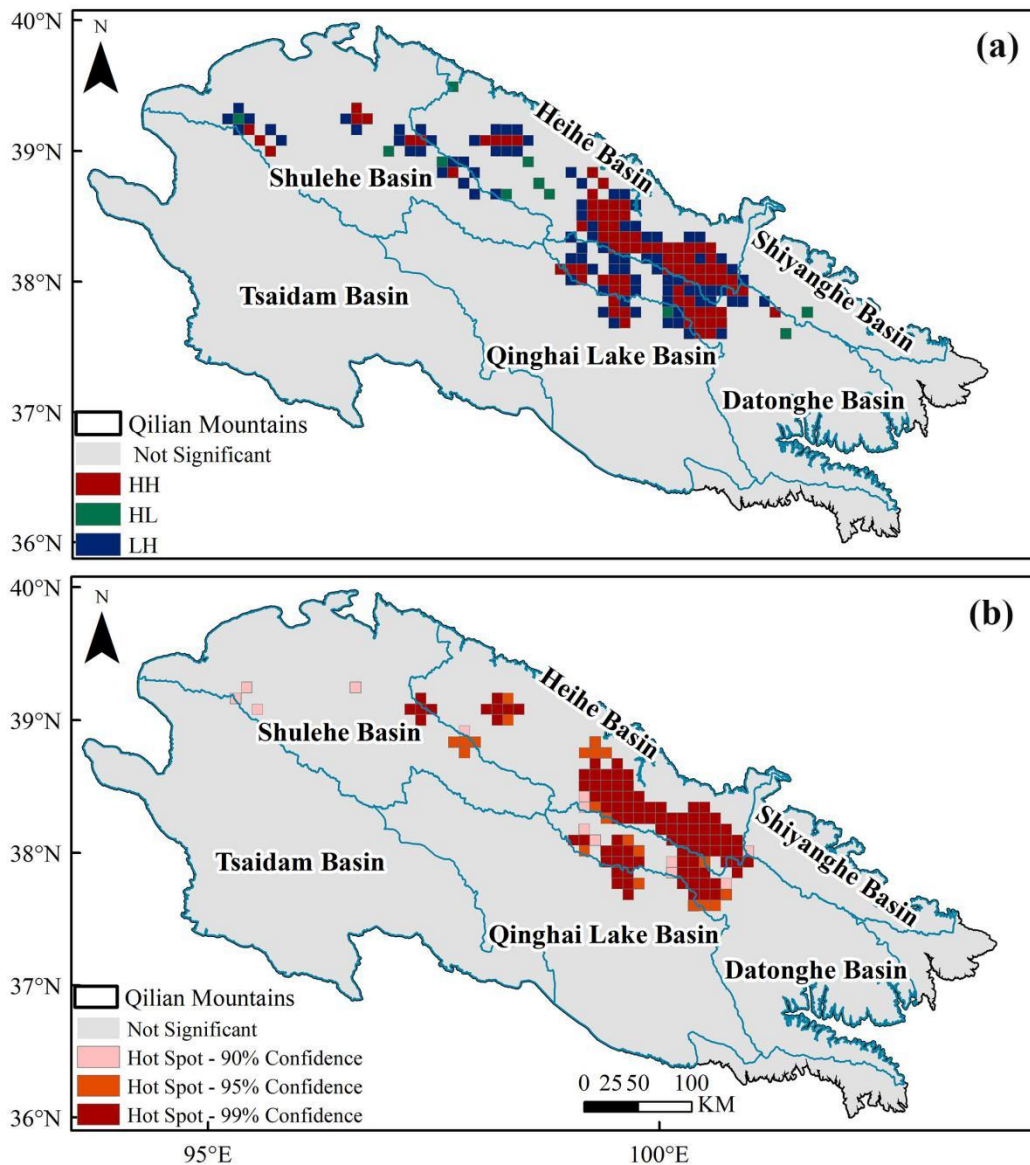
259 Our inventory of HT includes the Heihe Basin, Shulehe Basin, Datonghe Basin,
260 Shiyanghe Basin, Qinghai Lake Basin, and Tsaidam Basin within the Qilian
261 Mountains, with a total of 1064 HT features. In any 100 km² grid cell, the maximum
262 density of HT is 63 (Figure 2). This density is lower than the 68 per 25 km² in the
263 central Tibetan Plateau reported by (Luo et al., 2022) and 88 per 25 square km² on
264 Banks Island, Canada from (Lewkowicz and Way, 2019). 67% of these HT features
265 were identified in the Heihe River basin, followed by the Datonghe River Basin,
266 accounting for 19%. The HT distribution in these river basins is irregular,
267 corroborated by a positive statistically significant Moran's index value of 0.3, p-value
268 of 0.00001 and z-score of 32.5. Of all the HT features, the largest is 58 ha, the
269 smallest area is 0.01 ha, with most being smaller than 10 ha. The average area is 1.75
270 ha, with a total area of 1708 ha.

271 The spatial distribution of RTS on the QTP is strongly controlled by terrain factors
272 such as the elevation, slope, TPI, and aspect (Luo et al., 2022). The statistical results
273 indicate that HT is observed at elevations ranging from 2,835 to 4,550 m. However,
274 90% of HTs are more likely to occur at elevations ranging from 3,200 to 4,000 m in
275 the middle/high elevation area of the Qilian Mountains. HT tends to occur on
276 north-facing slopes (Figure 3b and 3d), with slopes ranging from 3° to 25° (Figure 3c).
277 In addition, the TPI shows that ~85% of the HTs occur mainly between 0.5 and 0.8
278 (Figure 3a), suggesting that they commonly occur in locations that are lower than
279 their surroundings. Both LSI indices suggest that 75% of HT has values close to 1.0
280 (Figure 3e), indicating that most HT is simple in shape and compact in morphology
281 (Niu et al., 2016). Alpine meadow areas contain ~53% of HT, followed by alpine
282 scrub meadows, which contain 13% (Figure 3f).

283 The initiation years of HT features are variable across the study area. 187 HT features
284 (18%) were identified before 2010, and the remaining 82% in the last 10 years. 392
285 sites (37%) were initiated in 2010-2015 and 482 (45%) after 2015. Much of the newly
286 initiated HT occurred in the Heihe basin and the middle and upper reaches of the
287 Datonghe basin (Figure 4), which is also a HT hotspot region. The recent increase in
288 HT can be attributed to the anomalous weather conditions in the corresponding years.
289 The association between newly observed HT and meteorological data indicates a
290 sudden HT increase in years with unusually high temperatures during the thawing
291 season (Figure 6).



292
293 **Figure 4** The timing of HT initiation within 100 km² grid cells.



294
 295 **Figure 5** (a) Spatial auto-correlation indicating high-high (HH), high-low (HL), and
 296 low-high (LH) clustering, and (b) hotspot analysis where the different colors represent
 297 the confidence levels.

298
 299

6 Discussion

300 6.1 Drivers of HT in the Qilian Mountainous

301 6.1.1 Permafrost Conditions

302 Formation of HT is facilitated by thick subsurface ice and various internal and
 303 external environmental conditions (Stephani et al., 2023). Permafrost stability in
 304 ~80% of the permafrost area of the Qilian Mountains is predominantly transitional,
 305 and higher permafrost temperatures (Ran et al., 2021) will exacerbate the climate
 306 sensitivity of this area (Lewkowicz and Way, 2019; Patton et al., 2021) leading to
 307 melting of the subsurface ice and an increase in active layer thickness, thus decreasing
 308 the stability of the slope (Behnia and Blais-Stevens, 2018). This is also supported by
 309 our finding that ~90% of HT occurs in the transition zone between permafrost and

310 seasonally frozen soil where mean annual ground temperature is greater than -1°C .

311

312 *6.1.2 Environmental Factors*

313 Topographic conditions facilitate the formation of subsurface ice and the continuous
314 development of HT. At elevations below 5100 m on the QTP, aspect dominates the
315 distribution of permafrost. More permafrost underlies regions of shaded, north-facing
316 slopes than sunny south-facing slopes (Ran et al., 2021). Indeed, we find that $\sim 95\%$ of
317 Qilian Mountain HT is found on north-facing slopes where it also enhances vegetation
318 growth and soil moisture storage (Jin et al., 2009). Lower solar radiation, higher
319 permafrost ice content, and shallow active layer thickness (Lacelle et al., 2015; Ward
320 Jones et al., 2019) also enables HT formation (Luo et al., 2022; Niu et al., 2016; Xia
321 et al., 2022). We find more than half of the HT occurs in alpine meadows, which
322 require more water content than alpine steppes (Yin et al., 2017) and consequently
323 also results in more ground ice development under this vegetation type. We
324 determined that $\sim 90\%$ of HT in the Qilian Mountains occurs on 3° to 25° slopes. Low
325 and gentle slopes are favorable for groundwater pooling (Luo et al., 2022), whereas
326 slopes greater than 16° are relatively steep and therefore not conducive to
327 groundwater enrichment for ice formation, but such slopes also provide dynamic
328 conditions for active layer detachments and collapsing ground (Wang, 1990). We also
329 observe more HT initiation at locations that are lower compared to their surroundings,
330 as such depressions favor the accumulation of snow and rainwater (Stieglitz et al.,
331 2003) and prevent heat loss from the soil. This encourages melting of subsurface ice
332 (Zhang, 2005) at the base of the active layer and, after an unstable layer is formed
333 between the permafrost and the active layer, the overlying soil can slide along the
334 slope (Patton et al., 2021).

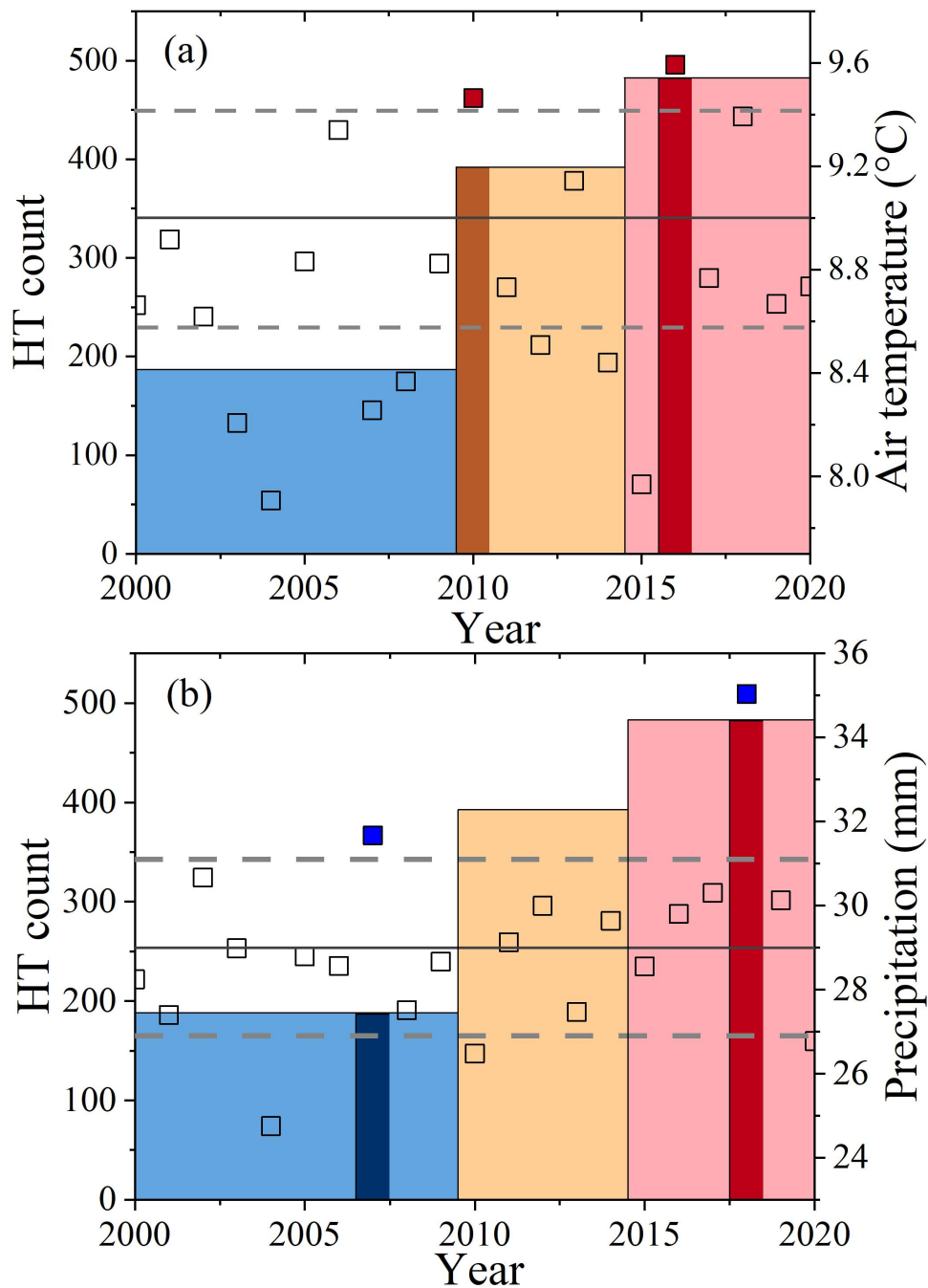
335 The Qilian Mountains were and are still formed by the ongoing collision of the Indian
336 Ocean Plate and the Eurasian Plate, resulting in the Qilian Mountains-Hexi Corridor
337 active fault system (Xiong et al., 2017) that has seen nearly 400 earthquakes of
338 magnitude 2 or greater over the past two decades. In particular, the high seismic
339 activity of the Heihe, Shiyanghe, and Datonghe Basins (Figure 7a) represents a
340 potential threat to the safety and integrity of current and future infrastructure in the
341 region. During our field investigations we found a nearly 3 km long and 2 m deep
342 slope fracture caused by a 6.9-magnitude earthquake in 2022, resulting in a massive
343 exposure of subsurface ice and the collapse of the Lanzhou-Xinjiang High Speed Rail
344 Tunnel (Figure 7b and c). The occurrence of an earthquake can result in an
345 instantaneous increase in pore water pressure and sliding forces that reduce slope
346 stability and potentially leads to a massive exposure of subsurface ice (Niu et al., 2016;
347 Xia et al., 2022), sediment liquefaction (Dadfar et al., 2017), and permafrost warming
348 due to the seismic vibrations. These vibrations lead to cracking and deformation of the
349 ice layers within the permafrost, releasing moisture and heat, consequently resulting
350 in a temperature rise of the permafrost. Additionally, earthquakes can induce the flow
351 of pore water within the permafrost, further influencing its temperature (Che et al.,
352 2014), creating the ideal setting for active-layer detachment slides. The clustering of
353 earthquake activity in the lower left corner of Figure 7a is not associated with HT
354 features, because there is no permafrost in this region.

355

356 *6.1.3 Climate Factors*

357 Extreme summer temperatures and precipitation have been identified as triggers for
358 the initiation of RTSs in many Arctic permafrost zones (Balsler et al., 2014; Kokelj et

359 al., 2015; Lewkowicz and Way, 2019; Segal et al., 2016). Given our finding that 82%
360 of HT was initiated in the last decade (Figure 4), mostly during 2010-2015 and after
361 2015, we used ERA5 to determine the temperature and precipitation characteristics
362 for the Qilian Mountains over the last 20 years (Li et al., 2022b) (Figure 6, the square
363 symbols). The mean thawing season air temperatures in 2010 and 2016 were higher
364 than in other years (Figure 6a, red square symbols). A warming thaw season could
365 lead to thaw consolidation at the base of the active layer or to higher porewater
366 pressure in the transient thaw layer, reducing the effective shear strength, and causing
367 slope failure (Lewkowicz and Way, 2019). The anomalous air temperatures during the
368 thawing season could accelerate permafrost thaw and expose ice-rich permafrost, thus
369 leading to new HT (Figure 6a, dark brown and dark red bars, respectively). Rainfall
370 infiltration may transfer heat to the top layer of permafrost and induce melting of
371 ground ice in ice-rich transient layers, which would increase the porewater pressure at
372 the active layer-permafrost interface and thereby trigger formation of HT (Luo et al.,
373 2022). However, precipitation variability during the thawing season does not match
374 HT formation (Figure 6b). Despite high precipitation in both 2007 and 2018 (Figure
375 6b, blue squares), no initiation of HT was found to subsequently coincide with these
376 peaks (blue squares), and precipitation also does not explain the significant initiation
377 of HTs between 2010-2015, nor after 2015 (Figure 6b, yellow and red bars,
378 respectively). The same conclusion also applies to the other three sub-regions—Hoh
379 Xil Mountain, Maqu county, and Honglianghe—and it could be speculated that the
380 nature of the soils on the QTP may instead play a role (Luo et al., 2022).
381

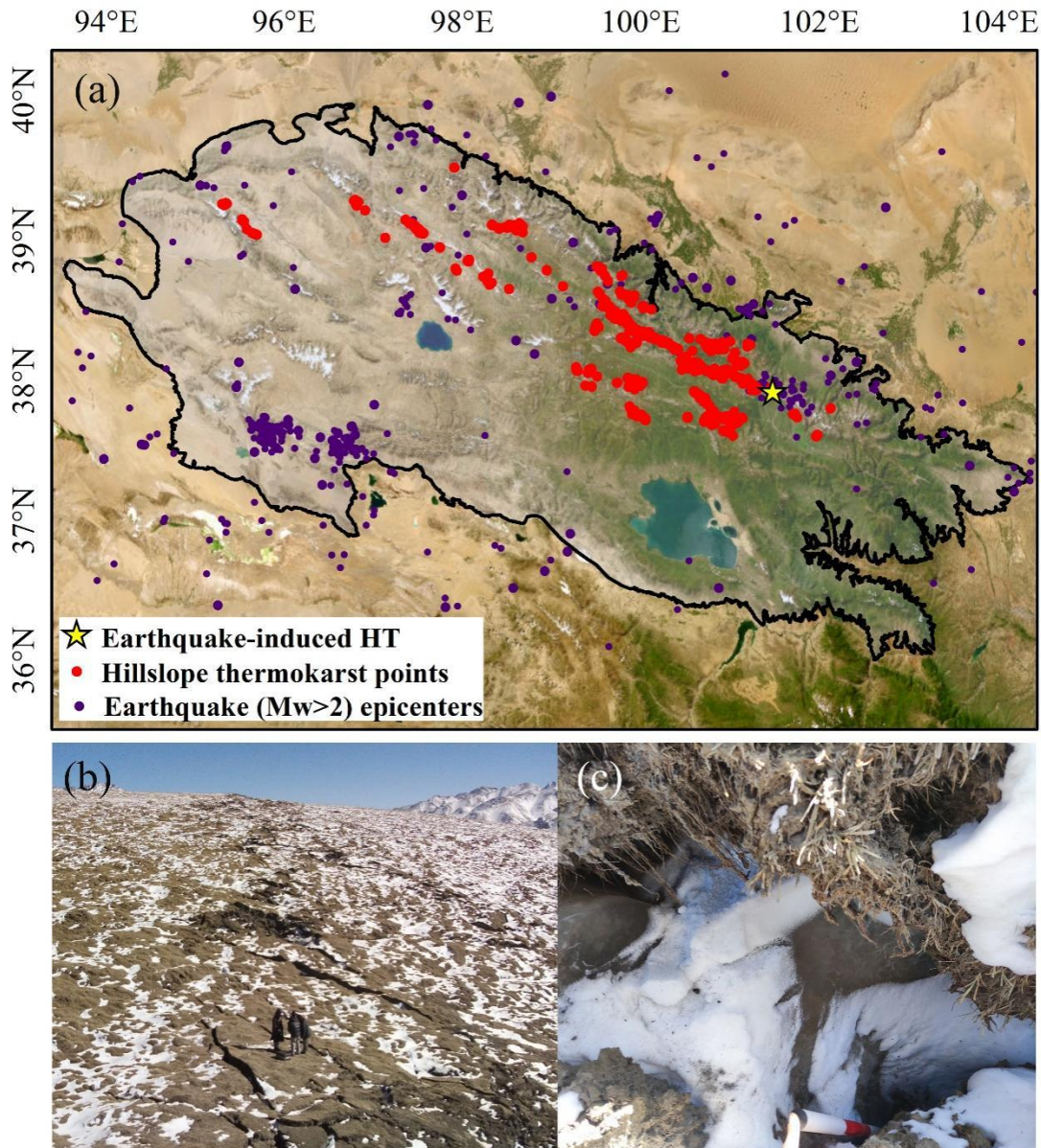


382
 383 **Figure 6** The relationship between HT numbers (unequal width bars, the darker colors
 384 represent years with extreme weather events.) and (a) temperature and (b)
 385 precipitation in the thawing season from 2000 to 2020 (square symbols, the red
 386 squares and the blue squares represent the extreme weather events.). The solid
 387 horizontal line represents the mean air temperature and precipitation, respectively, and
 388 the dashed line represents ± 1 standard deviation.

389
 390 *6.1.4 Human Activities*

391 Extensive and increasing human activities have been shown to significantly accelerate
 392 permafrost degradation (Cheng & Jin, 2013; IPCC, 2019). The total population of the
 393 Qilian Mountains is about 60,000, there are approximately 1,000 metal, energy, and
 394 other types of mineral deposits (National Mineral Properties Database 2021 Edition,

395 <http://data.ngac.org.cn/mineralresource/index.html>), and there are ~8,000 km of
 396 railroads and highways. The core of this human activity is concentrated on the eastern
 397 side of the Qilian Mountains, which generally coincides with the spatial distribution
 398 of the HT hotspots we documented. This qualitatively suggests a role of human
 399 activities on HT from, e.g., engineering disturbances, vegetation degradation due to
 400 overgrazing, etc. (Sharkhuu et al., 2007). Establishing the impact of human activities
 401 on HT quantitatively is still a difficult challenge, but our identification of the location
 402 and timing of HT formation is a first, important step for further future studies,
 403 especially on the socioeconomic development in the region.
 404



405 **Figure 7** Qilian Mountains showing (a) the location of HT locations and earthquakes
 406 with magnitude >2 in the last 20 years, (b) slope fractures caused by earthquakes, and
 407 (c) exposed subsurface ice.
 408

409

410 **7 Data Availability**

411 DEM data can be accessed through NASA

412 (<https://www.earthdata.nasa.gov/sensors/srtm>). Landsat5-8 data are available from
413 USGS (<https://www.usgs.gov/>) and Sentinel-2 from ESA (<https://www.esa.int/>), and
414 can be downloaded through Google Earth Engine. Esri World Imagery can be
415 accessed through Esri Wayback Imagery at: <https://livingatlas.arcgis.com/wayback>.
416 Some GF-2 imagery is also available online through Omap software
417 (<https://www.ovital.com/283-2/>), and high resolution 3D satellite imagery of the
418 Qilian Mountain region can be viewed in Google Earth software. High-resolution
419 satellite images captured by the Jilin-1 satellite in China can be viewed by accessing
420 <https://www.jl1mall.com/rskit/>. The HT inventory for the Qilian Mountains can be
421 freely downloaded from the National Tibetan Plateau/Third Pole Environment Data
422 Center (<https://doi.org/10.11888/Cryos.tpdc.300805>, Peng and Yang, 2023).

423

424 **8 Conclusion**

425 This study used visual interpretation and field investigations for repeated verification
426 to investigate HT in the permafrost zone of the Qilian Mountains. We successfully
427 produced the first HT inventory for this area, and found it contains a total of 1064 HT
428 features. The area of these features ranged from 0.01 to 58 ha, with an average of 1.75
429 ha. Thermokarst is primarily concentrated at the junction between the upstream
430 portion of the Heihe River Basin and the mid and upstream portion of the Datonghe
431 Basin. Within a 10×10 km area, thermokarst has a maximum density of 63 features,
432 affecting an area of ~20 km². HT in the Qilian Mountains is more likely to occur on
433 north-facing shaded slopes, at elevations between 3200–4000 m, slopes of 3–25°,
434 0.5<TPI<0.8, and in alpine meadow vegetation. Based on long-term satellite imagery,
435 874 new HT features were initiated after 2010, accounting for 82% of the total HT.
436 Recent higher air temperatures during the thawing season are likely important reasons
437 for the intensification of HT formation in the Qilian Mountains, while precipitation
438 does not seem to play a role. This first HT inventory for the Qilian Mountains will be
439 fundamental for quantitative assessments that explore the exact causes and underlying
440 thermokarst processes, and ultimately allow for better identification prediction of
441 areas prone to thermokarst formation in the future.

442

443 **Author contributions.** XP and GY designed the research and obtained funding. GY
444 analyzed the data and prepared the data files. GY, WT, XL and XP conducted the field
445 work. GY, XP, OWF, JL, CM, FN wrote the paper with input from the coauthors and
446 coordinated the analysis and contributions from all coauthors. XP and GY contributed
447 to the work equally and should be regarded as co-first authors.

448

449 **Competing interests.** The contact author has declared that neither they nor their
450 coauthors have any competing interests.

451

452 **Disclaimer.** Publisher's note: Copernicus Publications remains neutral with regard to
453 jurisdictional claims in published maps and institutional affiliations.

454

455 **Acknowledgements**

456 This work was supported by the Second Tibetan Plateau Scientific Expedition and
457 Research Program (STEP) (2019QZKK0905), the National Natural Science
458 Foundation of China (42161160328, 42171120), and the Fundamental Research
459 Funds for the Central Universities (lzujbky-2023-01).

460

461 **References**

- 462 Balsler, A. W., Jones, J. B., and Gens, R.: Timing of retrogressive thaw slump
463 initiation in the Noatak Basin, northwest Alaska, USA, *J. Geophys. Res. Earth Surf.*,
464 119, 1106–1120, <https://doi.org/10.1002/2013JF002889>, 2014.
- 465 Behnia, P. and Blais-Stevens, A.: Landslide susceptibility modelling using the
466 quantitative random forest method along the northern portion of the Yukon Alaska
467 Highway Corridor, Canada, *Nat. Hazards*, 90, 1407–1426,
468 <https://doi.org/10.1007/s11069-017-3104-z>, 2018.
- 469 Bivand, R. S. and Wong, D. W. S.: Comparing implementations of global and local
470 indicators of spatial association, *TEST*, 27, 716–748,
471 <https://doi.org/10.1007/s11749-018-0599-x>, 2018.
- 472 Che, A., Wu, Z., and Wang, P.: Stability of pile foundations base on warming effects
473 on the permafrost under earthquake motions, *Soils Found.*, 54, 639–647,
474 <https://doi.org/10.1016/j.sandf.2014.06.006>, 2014.
- 475 Chen, H., Zhu, Q., Peng, C., Wu, N., Wang, Y., Fang, X., Gao, Y., Zhu, D., Yang, G.,
476 Tian, J., Kang, X., Piao, S., Ouyang, H., Xiang, W., Luo, Z., Jiang, H., Song, X.,
477 Zhang, Y., Yu, G., Zhao, X., Gong, P., Yao, T., and Wu, J.: The impacts of climate
478 change and human activities on biogeochemical cycles on the Qinghai-Tibetan
479 Plateau, *Glob. Change Biol.*, 19, 2940–2955, <https://doi.org/10.1111/gcb.12277>, 2013.
- 480 Cheng, G. and Jin, H.: Permafrost and groundwater on the Qinghai-Tibet Plateau and
481 in northeast China, *Hydrogeol. J.*, 21, 5–23,
482 <https://doi.org/10.1007/s10040-012-0927-2>, 2013.
- 483 Dadfar, B., El Naggar, M. H., and Nastev, M.: Quantifying exposure of linear
484 infrastructures to earthquake-triggered transverse landslides in permafrost thawing
485 slopes, *Can. Geotech. J.*, 54, 1002–1012, <https://doi.org/10.1139/cgj-2017-0076>,
486 2017.
- 487 Farr, T. G., Rosen, P. A., Caro, E., Crippen, R., Duren, R., Hensley, S., Kobrick, M.,
488 Paller, M., Rodriguez, E., Roth, L., Seal, D., Shaffer, S., Shimada, J., Umland, J.,
489 Werner, M., Oskin, M., Burbank, D., and Alsdorf, D.: The Shuttle Radar Topography
490 Mission, *Rev. Geophys.*, 45, <https://doi.org/10.1029/2005RG000183>, 2007.
- 491 Gooseff, M. N., Balsler, A., Bowden, W. B., and Jones, J. B.: Effects of Hillslope
492 Thermokarst in Northern Alaska, *Eos Trans. Am. Geophys. Union*, 90, 29–30,
493 <https://doi.org/10.1029/2009EO040001>, 2009.
- 494 Huang, L., Luo, J., Lin, Z., Niu, F., and Liu, L.: Using deep learning to map
495 retrogressive thaw slumps in the Beiluhe region (Tibetan Plateau) from CubeSat
496 images, *Remote Sens. Environ.*, 237, 111534,
497 <https://doi.org/10.1016/j.rse.2019.111534>, 2020.
- 498 Huang, L., Willis, M. J., Li, G., Lantz, T. C., Schaefer, K., Wig, E., Cao, G., and
499 Tiampo, K. F.: Identifying active retrogressive thaw slumps from ArcticDEM, *ISPRS*
500 *Journal of Photogrammetry and Remote Sensing*, 205, 301–316,
501 <https://doi.org/10.1016/j.isprsjprs.2023.10.008>, 2023.

- 502 Jin, H., Li, X., Frauenfeld, O. W., Zhao, Y., Chen, C., Du, R., Du, J., and Peng, X.:
503 Comparisons of statistical downscaling methods for air temperature over the Qilian
504 Mountains, *Theor. Appl. Climatol.*, 149, 893–896,
505 <https://doi.org/10.1007/s00704-022-04081-w>, 2022.
- 506 Jin, X., Wan, L., Zhang, Y.-K., Hu, G., Schaepman, M. E., Clevers, J. G. P. W., and Su,
507 Z. B.: Quantification of spatial distribution of vegetation in the Qilian Mountain area
508 with MODIS NDVI, *Int. J. Remote Sens.*, 30, 5751–5766,
509 <https://doi.org/10.1080/01431160902736635>, 2009.
- 510 Kokelj, S. V., Tunnicliffe, J., Lacelle, D., Lantz, T. C., Chin, K. S., and Fraser, R.:
511 Increased precipitation drives mega slump development and destabilization of ice-rich
512 permafrost terrain, northwestern Canada, *Glob. Planet. Change*, 129, 56–68,
513 <https://doi.org/10.1016/j.gloplacha.2015.02.008>, 2015.
- 514 Kokelj, S. V. and Jorgenson, M. T.: Advances in Thermokarst Research: Recent
515 Advances in Research Investigating Thermokarst Processes, Permafrost and Periglac.
516 *Process.*, 24, 108–119, <https://doi.org/10.1002/ppp.1779>, 2013.
- 517 Lacelle, D., Brooker, A., Fraser, R. H., and Kokelj, S. V.: Distribution and growth of
518 thaw slumps in the Richardson Mountains–Peel Plateau region, northwestern Canada,
519 *Geomorphology*, 235, 40–51, <https://doi.org/10.1016/j.geomorph.2015.01.024>, 2015.
- 520 Lantuit, H. and Pollard, W. H.: Fifty years of coastal erosion and retrogressive thaw
521 slump activity on Herschel Island, southern Beaufort Sea, Yukon Territory, Canada,
522 *Geomorphology*, 95, 84–102, <https://doi.org/10.1016/j.geomorph.2006.07.040>, 2008.
- 523 Lantz, T. C. and Kokelj, S. V.: Increasing rates of retrogressive thaw slump activity in
524 the Mackenzie Delta region, N.W.T., Canada, *Geophys. Res. Lett.*, 35, L06502,
525 <https://doi.org/10.1029/2007GL032433>, 2008.
- 526 Lewkowicz, A. G.: Dynamics of active-layer detachment failures, Fosheim Peninsula,
527 Ellesmere Island, Nunavut, Canada, *Permafrost Periglac. Process.*, 18, 89–103,
528 <https://doi.org/10.1002/ppp.578>, 2007.
- 529 Lewkowicz, A. G. and Way, R. G.: Extremes of summer climate trigger thousands of
530 thermokarst landslides in a High Arctic environment, *Nat. Commun.*, 10, 1329,
531 <https://doi.org/10.1038/s41467-019-09314-7>, 2019.
- 532 Li, Y., Qin, X., Liu, Y., Jin, Z., Liu, J., Wang, L., and Chen, J.: Evaluation of
533 Long-Term and High-Resolution Gridded Precipitation and Temperature Products in
534 the Qilian Mountains, Qinghai–Tibet Plateau, *Front. Environ. Sci.*, 10, 906821,
535 <https://doi.org/10.3389/fenvs.2022.906821>, 2022.
- 536 Luo, J., Niu, F., Lin, Z., Liu, M., and Yin, G.: Thermokarst lake changes between
537 1969 and 2010 in the Beilu River Basin, Qinghai–Tibet Plateau, China, *Sci. Bull.*, 60,
538 556–564, <https://doi.org/10.1007/s11434-015-0730-2>, 2015.
- 539 Luo, J., Niu, F., Lin, Z., Liu, M., and Yin, G.: Recent acceleration of thaw slumping in
540 permafrost terrain of Qinghai-Tibet Plateau: An example from the Beiluhe Region,
541 *Geomorphology*, 341, 79–85, <https://doi.org/10.1016/j.geomorph.2019.05.020>, 2019.

- 542 Luo, J., Niu, F., Lin, Z., Liu, M., Yin, G., and Gao, Z.: Inventory and Frequency of
 543 Retrogressive Thaw Slumps in Permafrost Region of the Qinghai–Tibet Plateau,
 544 *Geophys. Res. Lett.*, 49, <https://doi.org/10.1029/2022GL099829>, 2022.
- 545 Mu, C., Shang, J., Zhang, T., Fan, C., Wang, S., Peng, X., Zhong, W., Zhang, F., Mu,
 546 M., and Jia, L.: Acceleration of thaw slump during 1997–2017 in the Qilian
 547 Mountains of the northern Qinghai-Tibetan plateau, *Landslides*, 17, 1051–1062,
 548 <https://doi.org/10.1007/s10346-020-01344-3>, 2020.
- 549 Muster, S., Roth, K., Langer, M., Lange, S., Cresto Aleina, F., Bartsch, A.,
 550 Morgenstern, A., Grosse, G., Jones, B., Sannel, A. B. K., Sjöberg, Y., Günther, F.,
 551 Andresen, C., Veremeeva, A., Lindgren, P. R., Bouchard, F., Lara, M. J., Fortier, D.,
 552 Charbonneau, S., Virtanen, T. A., Hugelius, G., Palmtag, J., Siewert, M. B., Riley, W.
 553 J., Koven, C. D., and Boike, J.: PeRL: a circum-Arctic Permafrost Region Pond and
 554 Lake database, *Earth Syst. Sci. Data*, 9, 317–348,
 555 <https://doi.org/10.5194/essd-9-317-2017>, 2017.
- 556 Nitze, I., Grosse, G., Jones, B. M., Romanovsky, V. E., and Boike, J.: Remote sensing
 557 quantifies widespread abundance of permafrost region disturbances across the Arctic
 558 and Subarctic, *Nat. Commun.*, 9, 5423, <https://doi.org/10.1038/s41467-018-07663-3>,
 559 2018.
- 560 Niu, F., Luo, J., Lin, Z., Liu, M., and Yin, G.: Morphological Characteristics of
 561 Thermokarst Lakes along the Qinghai-Tibet Engineering Corridor, *Arct. Antarct. Alp.*
 562 *Res.*, 46, 963–974, <https://doi.org/10.1657/1938-4246-46.4.963>, 2014.
- 563 Niu, F., Luo, J., Lin, Z., Fang, J., and Liu, M.: Thaw-induced slope failures and
 564 stability analyses in permafrost regions of the Qinghai-Tibet Plateau, China,
 565 *Landslides*, 13, 55–65, <https://doi.org/10.1007/s10346-014-0545-2>, 2016.
- 566 Nicu, I. C., Lombardo, L., and Rubensdotter, L.: Preliminary assessment of thaw
 567 slump hazard to Arctic cultural heritage in Nordenskiöld Land, Svalbard, *Landslides*,
 568 18, 2935–2947, <https://doi.org/10.1007/s10346-021-01684-8>, 2021.
- 569 Nicu, I. C., Elia, L., Rubensdotter, L., Tanyaş, H., and Lombardo, L.: Multi-hazard
 570 susceptibility mapping of cryospheric hazards in a high-Arctic environment: Svalbard
 571 Archipelago, *Earth Syst. Sci. Data*, 15, 447–464,
 572 <https://doi.org/10.5194/essd-15-447-2023>, 2023.
- 573 Olefeldt, D., Goswami, S., Grosse, G., Hayes, D., Hugelius, G., Kuhry, P., McGuire,
 574 A. D., Romanovsky, V. E., Sannel, A. B. K., Schuur, E. A. G., and Turetsky, M. R.:
 575 Circumpolar distribution and carbon storage of thermokarst landscapes, *Nat.*
 576 *Commun.*, 7, 13043, <https://doi.org/10.1038/ncomms13043>, 2016.
- 577 Patton, A. I., Rathburn, S. L., Capps, D. M., McGrath, D., and Brown, R. A.: Ongoing
 578 Landslide Deformation in Thawing Permafrost, *Geophys. Res. Lett.*, 48,
 579 <https://doi.org/10.1029/2021GL092959>, 2021.
- 580 Peng, X. and Yang, G.: The hillslope thermokarst inventory for the permafrost region
 581 of the Qilian Mountains (2000–2020). National Tibetan Plateau Data Center[data set],
 582 <https://doi.org/10.11888/Cryos.tpd.c.300805>, 2023.

- 583 Ran, Y., Li, X., Cheng, G., Nan, Z., Che, J., Sheng, Y., Wu, Q., Jin, H., Luo, D., Tang,
584 Z., and Wu, X.: Mapping the permafrost stability on the Tibetan Plateau for
585 2005–2015, *Sci. China Earth Sci.*, 64, 62–79,
586 <https://doi.org/10.1007/s11430-020-9685-3>, 2021.
- 587 Segal, R. A., Lantz, T. C., and Kokelj, S. V.: Acceleration of thaw slump activity in
588 glaciated landscapes of the Western Canadian Arctic, *Environ. Res. Lett.*, 11, 034025,
589 <https://doi.org/10.1088/1748-9326/11/3/034025>, 2016.
- 590 Sharkhuu, A., Sharkhuu, N., Eitzelmüller, B., Heggem, E. S. F., Nelson, F. E.,
591 Shiklomanov, N. I., Goulden, C. E., and Brown, J.: Permafrost monitoring in the
592 Hovsgol mountain region, Mongolia, *J. Geophys. Res.*, 112, F02S06,
593 <https://doi.org/10.1029/2006JF000543>, 2007.
- 594 Stephani, E., Darrow, M. M., Kanevskiy, M., Wuttig, F., Daanen, R. P., Schwarber, J.
595 A., Doré, G., Shur, Y., Jorgenson, M. T., Croft, P., and Drage, J. S.: Hillslope erosional
596 features and permafrost dynamics along infrastructure in the Arctic Foothills, Alaska,
597 *Permafr. Periglac. Process.*, 34, 208–228, <https://doi.org/10.1002/ppp.2188>, 2023.
- 598 Stieglitz, M., Déry, S. J., Romanovsky, V. E., and Osterkamp, T. E.: The role of snow
599 cover in the warming of arctic permafrost, *Geophys. Res. Lett.*, 30,
600 <https://doi.org/10.1029/2003GL017337>, 2003.
- 601 Wang, R., Peng, Q., Zhang, W., Zhao, W., Liu, C., and Zhou, L.: Ecohydrological
602 Service Characteristics of Qilian Mountain Ecosystem in the Next 30 Years Based on
603 Scenario Simulation, *Sustainability*, 14, 1819, <https://doi.org/10.3390/su14031819>,
604 2022.
- 605 Ward Jones, M. K., Pollard, W. H., and Jones, B. M.: Rapid initialization of
606 retrogressive thaw slumps in the Canadian high Arctic and their response to climate
607 and terrain factors, *Environ. Res. Lett.*, 14, 055006,
608 <https://doi.org/10.1088/1748-9326/ab12fd>, 2019.
- 609 Xia, Z., Huang, L., Fan, C., Jia, S., Lin, Z., Liu, L., Luo, J., Niu, F., and Zhang, T.:
610 Retrogressive thaw slumps along the Qinghai–Tibet Engineering Corridor: a
611 comprehensive inventory and their distribution characteristics, *Earth Syst. Sci. Data*,
612 14, 3875–3887, <https://doi.org/10.5194/essd-14-3875-2022>, 2022.
- 613 Xiong, J., Li, Y., Zhong, Y., Lu, H., Lei, J., Xin, W., Wang, L., Hu, X., and Zhang, P.:
614 Latest Pleistocene to Holocene Thrusting Recorded by a Flight of Strath Terraces in
615 the Eastern Qilian Shan, NE Tibetan Plateau, *TECTONICS*, 36, 2973–2986,
616 <https://doi.org/10.1002/2017TC004648>, 2017.
- 617 Yang, D., Qiu, H., Ye, B., Liu, Y., Zhang, J., and Zhu, Y.: Distribution and Recurrence
618 of Warming-Induced Retrogressive Thaw Slumps on the Central Qinghai-Tibet
619 Plateau, *J. Geophys. Res. Earth Surf.*, 128, e2022JF007047,
620 <https://doi.org/10.1029/2022JF007047>, 2023.
- 621 Yin, G., Niu, F., Lin, Z., Luo, J., and Liu, M.: Effects of local factors and climate on
622 permafrost conditions and distribution in Beiluhe basin, Qinghai-Tibet Plateau, China,
623 *Sci. Total Environ.*, 581–582, 472–485,

- 624 <https://doi.org/10.1016/j.scitotenv.2016.12.155>, 2017.
- 625 Yin, G., Luo, J., Niu, F., Lin, Z., and Liu, M.: Machine learning-based thermokarst
626 landslide susceptibility modeling across the permafrost region on the Qinghai-Tibet
627 Plateau, *Landslides*, 18, 2639–2649, <https://doi.org/10.1007/s10346-021-01669-7>,
628 2021.
- 629 YU Hong, J. Z., ZENG Hui: Study on Distribution Characteristics of Landscape
630 Elements along the Terrain Gradient, *SCIENTIA GEOGRAPHICA SINICA*, 21, 64,
631 <https://doi.org/10.13249/j.cnki.sgs.2001.01.64>, 2001.
- 632 Zhang, T.: Influence of the seasonal snow cover on the ground thermal regime: An
633 overview, *Rev. Geophys.*, 43, <https://doi.org/10.1029/2004RG000157>, 2005.
- 634